Research Article | Vol. 34, No. 12 / 15 Jun 2026 / Optics Express 22163

Optics EXPRESS

2D approximation quickly breaks down in reflection ptychography

Sander Senhorst,[1,*] Stefan Witte,[1] and Wim Coene[1,2]

[1] *Department of Imaging Physics, Delft University of Technology, Lorentzweg 1, 2628 CJ Delft, The Netherlands*
[2] *ASML Netherlands B.V., De Run 6501, 5504 DR Veldhoven, The Netherlands*
[*] *s.senhorst@tudelft.nl*

Abstract: Ptychographic reconstructions in reflection geometries are commonly interpreted with the same two-dimensional thin-sample model used in transmission, yet the validity of this approximation has not been established. We develop a three-dimensional weak-scattering description of reflection ptychography and derive explicit thickness criteria for when a two-dimensional model remains accurate. Because the sampled axial spatial frequency range is dominated by the rotation of the Ewald sphere rather than its curvature, reflection geometries impose far stricter thin-sample conditions than transmission geometries. The allowable thickness is reduced by one to two orders of magnitude for a representative extreme ultraviolet geometry, depending on the tolerance for the appearance of artifacts. Simulations verify that conventional two-dimensional reconstructions may exhibit the thickness-dependent artifacts as predicted by the theory, with particularly strong distortions near specular Bragg minima. We further show that incorporating the correct depth-dependent propagation into the forward model resolves these distortions and enables recovery of sample thickness. These results establish practical validity limits for two-dimensional reflection ptychography and identify a path toward quantitative depth-sensitive reconstructions at all geometries.

1. Introduction

High-resolution imaging of surface structures enables advancement in many areas of research and technology, such as the imaging of patterned nanostructures for the field of lithography. As lithographic functional designs are set to create samples of interest with ever smaller lateral features, stacked on increasingly taller stacks [1], ptychography in reflection geometries, specifically at extreme ultraviolet (EUV) wavelengths around 13.5 nm, has emerged as a potential imaging solution that could tackle the needs of metrology and inspection for future lithographic processing nodes.

Ptychography is a form of coherent diffractive imaging (CDI), where a coherent probe beam is scanned across a sample, while at each scanning position a diffraction pattern is recorded [2,3]. If the scanning is performed with sufficient overlap in the illumination of adjacent probe beam positions, the resulting collection of diffraction patterns provides enough redundancy in the data to over-constrain the otherwise ill-posed inverse problem of reconstruction of the sample function from the data. This process, known as lensless imaging, enables the reconstruction of sample images at diffraction-limited lateral resolutions without the requirement of diffraction-limited optical components. Ptychography is of special benefit in application domains where use of diffraction-limited optics is prohibitive due to high cost or difficulty in manufacturing, such as in the domain of imaging using extreme ultraviolet wavelengths.

Since many structures of interest are placed on substrates which are optically opaque, either due to thickness or strong absorption, it is often not possible to measure sufficient scattered intensity

#601179 https://doi.org/10.1364/OE.601179
Journal © 2026 Received 8 Apr 2026; revised 22 May 2026; accepted 23 May 2026; published 8 Jun 2026

Optics EXPRESS

in the transmission direction, so for such samples one must resort to imaging in a reflection-type geometry. An additional complication for EUV wavelengths is that the reflection coefficients only become significant at near-grazing incidence angles. For this reason, the angle of incidence on the sample is often chosen in the $(60°, 85°)$-degree range [4,5], leading to the additional complication of diffraction-pattern distortion. The theory of ptychography was originally developed for the transmission geometry [6]. For reflection geometries, its mathematical validity was never verified, despite many experimental demonstrations of its feasibility [4,5,7–22].

In many of the experimental demonstrations of reflection ptychography the reconstruction phase is converted to the height by means of the optical path difference and phase shift upon reflection [16,17], thus modeling the effect of depth in the sample as a constant phase shift in real space. Such an approach is based on the approximation that considers single incoming and outgoing wavevectors. The bounds of this approximation are however not clearly defined. By its nature, ptychography requires a range of incoming and outgoing wavevectors to generate diversity in the detected intensity, e.g. to create a focused illumination probe. Such a model can therefore only be completely correct if all incoming and outgoing wavevectors feel an approximately constant phase shift due to sample height, which should hold only in the limit of small detection and illumination numerical apertures. Some attempts have been made to model the effect of depth in reflection ptychography [23], which models layers as incoherent contributions, requiring explicit filtering of interference terms through spatial separation, and therefore only works for large thicknesses, such as modeling the reflection from the bottom of a subtrate.

In this work, we develop a theory that can model the effect of depth with explicit bounds on the maximal permissible thickness, using the same foundational assumption of weak scattering as the original ptychographic theory. Our developed theory predicts that distortions appear in reconstructions that are performed without adequately incorporating depth effects, which we verify in simulation. Finally, we show that more accurately incorporating the effect of depth in the ptychographic model can allow reconstruction of the feature thickness of binary lithographic samples using the propagation geometry alone.

2. 2D ptychographic model

In 2D scanning ptychographic reconstructions assumes the separability of the field ψ emerging from the sample of interest as the product of two parts: one which is independent with respect to the applied shift vector $\boldsymbol{R}_k$ at positional index k, and the other which is translated with respect to $\boldsymbol{R}_k$, i.e.

$$\psi_k(\boldsymbol{r}) = O(\boldsymbol{r} - \boldsymbol{R}_k)P(\boldsymbol{r}), \tag{1}$$

where in this case we have taken the "object" function O to be the shifting part, and the "probe" function of the illumination P to be the independent part.

If the measurement is performed in the Fraunhofer regime, we detect the intensity I_k of the Fourier transform of the exit field ψ_k, i.e:

$$I_k(\boldsymbol{\xi}) = |\tilde{\psi}_k|^2 = |\mathcal{F}_2\left\{\psi_k\right\}|^2, \tag{2}$$

where $\boldsymbol{\xi}$ is the reciprocal space coordinate measured by the detector and the tilde is used two-dimensional functions in reciprocal space, with the two-dimensional Fourier transform represented by $\mathcal{F}_2$. For the benefit of the reader, we have included an overview of notation conventions and key symbols in the Supplement 1.

Purely two-dimensional samples such as O in Eq. (1) exist only in theory, yet the preceding analysis is purely two-dimensional in both the real space ($\boldsymbol{r}$) and reciprocal space ($\boldsymbol{\xi}$) coordinates.

3. Transmission and reflection geometries

Before continuing with derivations, it is of benefit to already define specific geometries of our interest as this may aid in the visualisations by means of example. These geometries are the transmission and reflection geometries, which we parameterize in terms of

- the central illumination wavevector $\boldsymbol{k}_{i,0} = k_0(\sin\theta_i, 0, \cos\theta_i)$,
- the largest angle $\Delta\theta_i$ away from $\boldsymbol{k}_{i,0}$ such that the illumination numerical aperture $\mathrm{NA}_i = \sin\Delta\theta_i$,
- the central detection wavevector $\boldsymbol{k}_{d,0} = k_0(\sin\theta_d, 0, \cos\theta_d)$ corresponding to the plane wave that travels from the origin to the center of a detector placed in the far-field and
- the largest angle $\Delta\theta_d$ away from $\boldsymbol{k}_{d,0}$ such that the detection numerical aperture $\mathrm{NA}_d = \sin\Delta\theta_d$,

where θ_i and θ_d are the angles with respect to the z-axis.

Defining a transmission geometry is easily done by simply take any geometry where $\theta_i = \theta_d$. For simplicity we choose $\theta_i = \theta_d = 0$ such that the the central direction of incidence is aligned with the z-coordinate. The detected part of the exit field is then propagating in the same z-direction as the illumination part. Choosing $\theta_i = \theta_d \neq 0$ will influence the requirements on the thickness later on, but only because we will define the thickness t defined non-rotated coordinates. Such an experimental geometry is not usually very practical, so we disregard it in further analysis.

Reflection geometries are less trivial to define, since they require assumptions about the sample. What is commonly understood to be a *reflection geometry* is perhaps more aptly named as a *specular reflection geometry*. To define a specular reflection geometry we require the sample to have a single planar orientation, say with normal vector $\hat{\boldsymbol{s}}$, which dominates the total back-scattered intensity. This makes it natural to place the detector such that $\boldsymbol{k}_{d,0} \cdot \hat{\boldsymbol{s}} = \boldsymbol{k}_{i,0} \cdot \hat{\boldsymbol{s}}$, since in this way the central pixel of a far-field detector is generally also the brightest. Later on in our analysis, the difference in between the incoming and outgoing wavevectors will play an important role, so we already note that we can also write $(\boldsymbol{k}_{d,0} - \boldsymbol{k}_{i,0}) \parallel \hat{\boldsymbol{s}}$. If we assume we are dealing with such a sample, and we define the z-axis of our coordinate system to be along $-\hat{\boldsymbol{s}}$, then a *specular reflection geometry* is defined given by $\theta_d = \pi - \theta_i$. The two different geometries are schematically shown in Fig. 1.

Samples which are (approximally) flat with a sharp transitions along interfaces clearly possess a single normal vector $\hat{\boldsymbol{s}}$ perpendicular to their flat surfaces. General samples may not posess clear interface boundaries, or have sharp boundaries oriented along many different directions instead of a single direction. For such samples, there is no particular preferred placement of the detector with respect to the incoming direction. In such a case, one may still follow the analysis by setting $\boldsymbol{k}_{d,0}$ parallel to the vector between the origin and the central pixel of the detector placement of choice, and one is free to choose the coordinate system.

4. Fully three-dimensional description of wave propagation

In a fully three-dimensional approach, the probe P and object O functions are not completely equivalent. Since the probe function corresponds to an illuminating field, under conventionally made assumptions it should be a propagating solution to the homogenous scalar Helmholtz equation. An expression for the probe function propagated to any z-coordinate as a function of

Optics EXPRESS

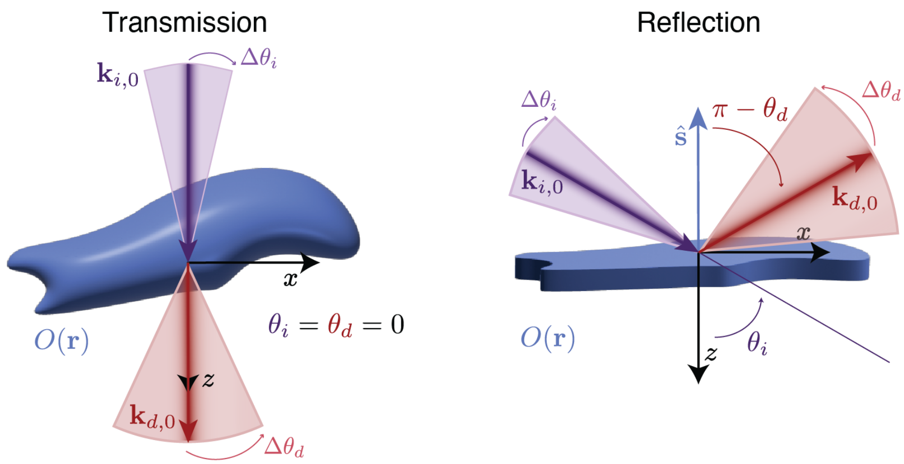

Fig. 1. The definition of the transmission geometry (left) and reflection geometry (right). The central wavevector of the illumination $\boldsymbol{k}_{i,0}$ is incident on the sample at an angle θ_i w.r.t. the z-axis, and the central wavevector of the detection $\boldsymbol{k}_{d,0}$ is emerging from the sample at an angle θ_d with respect to the z-axis. The range of the incoming wavevectors is indicated by $\Delta\theta_i$ and $\Delta\theta_d$, such that $\mathrm{NA}_{i/d} = \sin(\Delta\theta_{i/d})$. The sample in the transmission geometry may be any function, while the definition of the reflection geometry requires presence of the normal vector $\hat{\boldsymbol{s}}$ to define the direction of specular reflection.

field at $z = 0$ is well-known to be given by the angular spectrum propagator [24]

$$P(x, y, z) = \mathcal{F}_2^{-1} \left\{ \exp[\pm izk_z(\boldsymbol{\xi}_\perp)] \mathcal{F}_2 \left\{ P(x, y, z = 0) \right\} \right\}, \tag{3}$$

where $\boldsymbol{\xi}_\perp = (\xi_x, \xi_y)$ denote the transverse coordinates and where

$$k_z(\boldsymbol{\xi}_\perp) = k\sqrt{1 - \lambda^2\xi_x^2 - \lambda^2\xi_y^2}, \tag{4}$$

with wavenumber $k = 2\pi/\lambda$ for wavelength λ. The sign of the exponent in Eq. (3) must be chosen based on the propagation direction of the two-dimensional field; this sign is not uniquely constrained in the two-dimensional description. In a fully three-dimensional perspective, Eq. (3) may be written more concisely. Noting that the exponential factor is equivalent to the Fourier transform of a shifted impulse function of $\xi_z = \pm k_z(\boldsymbol{\xi}_\perp)$, the following expression is equivalent:

$$P(x, y, z) = \mathcal{F}_3^{-1} \left\{ \delta_{ES}^{\pm}(\boldsymbol{\xi}) \frac{k_z(\xi_\perp)}{k} \mathcal{F}_2 \left\{ P(x, y, z = 0) \right\} \right\}, \tag{5}$$

where $\mathcal{F}_3$ denotes the three-dimensional Fourier transform and where we make use of a special spherical impulse function $\delta_{ES}^{\pm}(\boldsymbol{\xi})$ introduced by Onural [25]. The $\frac{k_z(\xi_\perp)}{k}$ factor compensates for the effect of the Jacobian of δ_{ES}. The subscript ES indicates that the delta function sifts over the Ewald sphere S on which time-harmonic scalar fields have to reside, defined by

$$|\boldsymbol{\xi}|^2 = \xi_x^2 + \xi_y^2 + \xi_z^2 = k^2. \tag{6}$$

In $\mathbb{R}^3$, $\delta_{ES}(\boldsymbol{\xi})$ is defined by the sifting property

$$\iiint_{\mathbb{R}^3} \delta_{ES}(\boldsymbol{\xi}) f(\boldsymbol{\xi}) d^3\boldsymbol{\xi} = \iint_S f(\boldsymbol{\xi}_{ES}) d^2\boldsymbol{\xi}_{ES}. \tag{7}$$

Both signs of $\delta_{ES}^{\pm}$ have a similar definition, only further restricting the sphere S to taking either the upper half sphere ($\xi_z \geq 0$) or lower half sphere ($\xi_z < 0$). Aside from some mathematical intricacies related to the Jacobian when integrating over this impulse function in three-dimensional space [25], δ_{ES} may be interpreted as constraining the space of all three-dimensional functions to those with reciprocal vectors that obey the Ewald sphere condition for propagating time-harmonic fields.

Equation (5) may be understood by means of the Fourier slice theorem [26], which states that if we slice an N-dimensional function along one dimension, $\mathcal{S}_N$, and then take its $(N-1)$-dimensional Fourier transform, $\mathcal{F}_{N-1}$, that operation is equivalent to first taking a full N-dimensional Fourier transform, $\mathcal{F}_N$ and projecting the result downward onto the $(N-1)$-dimensional plane by integrating over the sliced dimension, $\mathcal{P}_N$:

$$\mathcal{F}_{N-1}\mathcal{S}_N = \mathcal{P}_{N-1}\mathcal{F}_N. \tag{8}$$

Equation (5) effectively inverts the slicing operator by using knowledge that the function f is a Helmholtz propagating solution traveling in the $\pm z$-direction: This allows us to undo the projection operator by defining an extension operator $\mathcal{E}_N$ in the Fourier domain which satisfies

$$\mathcal{E}_N\mathcal{P}_{N-1} = I_N, \tag{9}$$

where $\mathcal{I}_N$ the identity operation. Then we may write:

$$\mathcal{F}_N^{-1}\mathcal{E}_N\mathcal{F}_{N-1}\mathcal{S}_N = I_N. \tag{10}$$

These operators match the operators in Eq. (5), where we identify the extension operator $\mathcal{E}_3 = \delta^{\pm}_{ES}(\boldsymbol{\xi})\frac{k_z(\xi_\perp)}{k}$.

This fully three-dimensional perspective favors a description in reciprocal space, since here we may make use of the sifting property of the impulse function. The entire reciprocal space is sparsely filtered out due to the 2D section of the Ewald sphere in 3D reciprocal space. We thus continue in the Fourier domain, denoting three-dimensional Fourier transforms of functions with the hat symbol (e.g. $\hat{f}$), two-dimensional transforms with the tilde (e.g. $\tilde{f}$) and one dimensional transform with the bar (e.g. $\bar{f}$). These conventions are also presented in the list of key symbols in the Supplement 1.

When regarding Eq. (5), we see that the sign choice for k_z only allows us to describe half of the total possible solutions simultaneously. Our two-dimensional slice does not intrinsically carry information on the sign of the propagation z-direction, which may be in either the positive or negative direction. Therefore a general field description requires two different two-dimensional probes, one of which travels in the positive z-direction (P^+) and another in the negative z-direction (P^-):

$$\hat{P}(\boldsymbol{\xi}) = \delta^{+}_{ES}(\boldsymbol{\xi})\tilde{P}^{+}(\boldsymbol{\xi}_\perp) + \delta^{-}_{ES}(\boldsymbol{\xi})\tilde{P}^{-}(\boldsymbol{\xi}_\perp). \tag{11}$$

In general, we recommend the mental model where the "true" probe is considered to be the fully three-dimensional function $\hat{P}$ confined to the sphere S, while only further restricting the allowed reciprocal vectors when the specific geometry or constraints demand it, for example by demands on the propagation direction or limited numerical aperture.

5. Weak scattering in three dimensions

We will use this three-dimensional perspective on wave propagation to compute a scattered field due to interaction with a sample of interest. The most general approach to scattering uses the fact that the Helmholtz equation with varying index of refraction acts as a linear operator that maps an incident field P to a scattered field ψ. Since both P and ψ must be propagating solutions, they can be described in the Fourier domain as two-dimensional functions on the Ewald Sphere. Any

Optics EXPRESS

linear operator can be written as an integral with a kernel function, so we may write for a general solution

$$\tilde{\psi}(\boldsymbol{\xi}_{\perp}) = \iint S(\boldsymbol{\xi}_{\perp}, \boldsymbol{\xi}'_{\perp})\tilde{P}(\boldsymbol{\xi}'_{\perp})d^2\boldsymbol{\xi}'_{\perp}. \tag{12}$$

In this formulation, the scattering kernel S is a function of both the incident field's coordinates $\boldsymbol{\xi}'_{\perp}$ and the scattered field coordinates $\boldsymbol{\xi}_{\perp}$, so each incident plane-wave component has its own scattering function. Unfortunately, it is very difficult if not impossible to find an analytical description of the full four-dimensional kernel S given a scattering sample's refractive index distribution $O(\boldsymbol{r})$. As we will see, it is possible to simplify the general kernel S to the point that we can find an analytical solution if we assume the sample to be weakly scattering.

Under the weak scattering approach, the probe is unperturbed by the object O, i.e. it is a propagating solution of the homogenous Helmholtz equation, so all the previously presented theory applies. We compute the scattered field using the first Born approximation, where the scattered field is taken as a simple product in real space:

$$\psi_k(x, y, z) = P(\boldsymbol{r})O(\boldsymbol{r} - \boldsymbol{R}_k), \tag{13}$$

where now $\boldsymbol{r}$ and $\boldsymbol{R}_k$ are three-dimensional vectors as opposed to the two-dimensional statement of Eq. (1). We note that standard ptychographic experiments will have $\boldsymbol{R}_k \cdot \hat{\boldsymbol{z}} = 0$, although this description does not require it. We should be careful however: Eq. (13) is only nearly correct, as it still includes those plane-wave components that correspond to modes which do not propagate to the far-field, i.e. it still contains modes which do not satisfy the Ewald sphere condition of Eq. (6). These non-propagating modes appear because, although P satisfies the Ewald sphere condition, O is any function of three variables, so their product in real space may fill the entire reciprocal space. A correct and quite concise statement is straightforward to make in reciprocal space using $\delta_{ES}(\boldsymbol{\xi})$,

$$\begin{aligned}\hat{\psi}_k(\boldsymbol{\xi}_d) &= \delta_{ES}(\boldsymbol{\xi}_d)\left[\hat{P} \circledast_3 \hat{O}_k\right](\boldsymbol{\xi}_d) \\ &= \delta_{ES}(\boldsymbol{\xi}_d) \iiint \hat{O}_k(\boldsymbol{\xi}_d - \boldsymbol{\xi}_i)\hat{P}(\boldsymbol{\xi}_i)d^3\boldsymbol{\xi}_i,\end{aligned} \tag{14}$$

where $\circledast_3$ denotes a three-dimensional convolution and we introduce the shorthand notation

$$\hat{O}_k(\boldsymbol{\xi}) = \mathcal{F}_3\{O(\boldsymbol{r} - \boldsymbol{R_k})\} = \hat{O}(\boldsymbol{\xi})\exp[i\boldsymbol{\xi} \cdot \boldsymbol{R}_k]. \tag{15}$$

We switch here to the label $\boldsymbol{\xi}_d$ for the coordinates of the exit field since these correspond to coordinates whose sampling will be determined geometrically by the placement of the detector. Equation (14) selects only outgoing or scattered waves that reside on the Ewald sphere of the same radius k, which means that we are assuming an elastically scattering sample with no energy loss. Additionally, it is an extension to the Fourier diffraction theorem (FDT) [27,28] first published by Wolf. The explicit coordinate relations from the original formulation, which arose by taking a plane-wave probe, are now implicit in the spherical impulse functions; furthermore, we immediately describe arbitrary incident fields. One should take special note of the scattering vector $\boldsymbol{q} = \boldsymbol{\xi}_d - \boldsymbol{\xi}_i$, which is especially relevant since it corresponds to the part of the three dimensional reciprocal space of the sample which is present in the convolution integral and which is thus "sampled" by the elastically scattered field. This vector may be recognizable to readers familiar with the theory of X-ray diffraction, where it often bears the name "diffraction vector". The effect of the convolution in Eq. (14) for the transmission and reflection geometry has been schematically shown in Fig. 2.

Optics EXPRESS

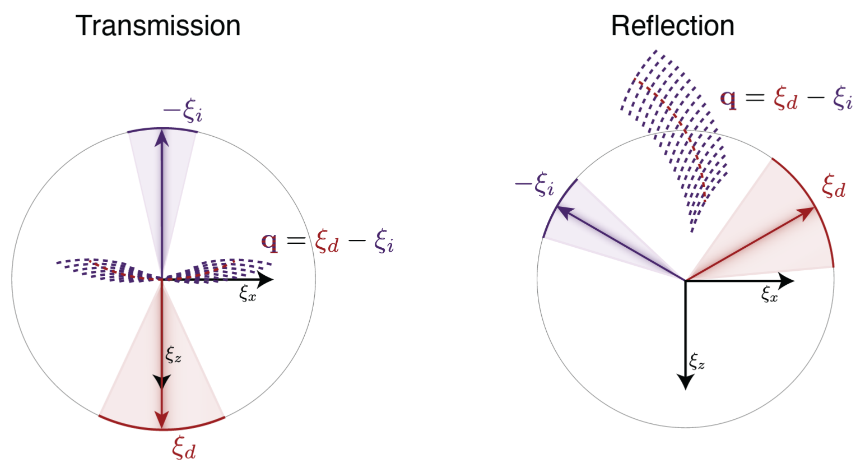

Fig. 2. The experimental geometry in the (ξ_x, ξ_z) Fourier plane. The dotted lines indicate all possible vectors $\boldsymbol{\xi}_d - \boldsymbol{\xi}_i$, and thus indicate the range of $\boldsymbol{q} = \boldsymbol{\xi}_d - \boldsymbol{\xi}_i$ in Eq. (14).

6. Cases for which two-dimensional descriptions fail

Having developed the fully three-dimensional perspective on weakly-scattering experiments, we may now use it to derive conditions where a two-dimensional approximation would be insufficient to reconstruct the ptychographic dataset. In other words, we will investigate conditions on the true, three-dimensional object function O for which it is possible to find two-dimensional functions $O'(x, y)$ and $P'(x, y)$ that produce nearly the same exit fields in the 2D ptychographic model as the the true functions O and P do in the fully 3D model. In this way, O' and P' are expected to be the solutions that are obtained when a 2D ptychographic solver is tasked with reconstructing a ptychographic dataset where the sample was actually three-dimensional. The approach will be the following: First we introduce the notion of thickness by considering "slab"-like objects whose 3D object function O is separable between the lateral (2D, $\perp = (x, y)$) and axial (1D, z) dimensions. For such objects, we find 2D functions $O'(x, y)$ and $P'(x, y)$ under various levels of strictness with regards to the object thickness. Then, using the reflection and transmission geometries defined previously, we derive explicit constraints on the maximal sample thickness for these specific geometries.

To introduce the notion of object thickness, we start out by separating the lateral object function from the effect of depth by assuming the object is separable, i.e.

$$O(x, y, z) = O_\perp(x, y) O_z(z). \tag{16}$$

Note that the separability in the real space also implies separability in Fourier space. The lateral part of the object function, $O_\perp$, will remain a general function that is to be retrieved by the ptychographic process. For the purpose of this analysis, the axial part of the object function, O_z, will take the role of imposing a finite sample thickness by restricting the 3D object O in the z dimension. It is worth noting however that this axial function might also be retrieved if it is adequately included in the ptychographic solver and the dataset has sufficient diversity.

The scattered field for the separable object is derived by inserting Eq. (16) into Eq. (14):

$$\hat{\psi}(\boldsymbol{\xi}_d) = \delta_{ES}(\boldsymbol{\xi}_d) \iiint \tilde{O}_\perp(\boldsymbol{\xi}_{d,\perp} - \boldsymbol{\xi}_{i,\perp}) \bar{O}_z(\xi_{d,z} - \xi_{i,z}) \hat{P}(\boldsymbol{\xi}_i) d^3\boldsymbol{\xi}_i. \tag{17}$$

One may compare this exit field to an exit field of purely a two-dimensional model, obtained by converting Eq. (1) to the Fourier domain for a single position, using our approximating P' and

Optics EXPRESS

O' functions:

$$\tilde{\psi}(\boldsymbol{\xi}_{d,\perp}) = \iint \tilde{O}'(\boldsymbol{\xi}_{d,\perp} - \boldsymbol{\xi}_{i,\perp})\tilde{P}'(\boldsymbol{\xi}_{i,\perp})d^2\boldsymbol{\xi}_{i,\perp}. \tag{18}$$

Since we are now working towards a 2D description again, for conciseness we will only consider an incident field traveling in the $+z$-direction $\tilde{P}^+$. A full description would be a sum of the positive and negative contributions. The scattered field (coordinate $\boldsymbol{\xi}_d$) on the other hand will be taken at both the positive and negative half sphere, as our goal is to compare transmission and reflection geometries, which will have opposite signs.

To obtain approximate equality between Eq. (17) and Eq. (18), we must turn the integration over 3 variables to an integration over 2 variables. One may note that the expression in Eq. (17) still has two delta functions present: one is hiding in $\hat{P}$ and the other is outside of the integration. We will now make use of the sifting property of these two delta functions to reduce the general three dimensional expression to a two-dimensional one.

First, we take the inverse Fourier transform along the z-axis. The sifting property of the delta function allows us to substitute $\xi_{d,z} = \pm k_z(\boldsymbol{\xi}_{d,\perp})$, and we obtain the additional Jacobian factor $k/k_z(\boldsymbol{\xi}_{d,\perp})$:

$$\begin{aligned}\tilde{\psi}(\boldsymbol{\xi}_{d,\perp}; z) &= \mathcal{F}_z^{-1}\left\{\hat{\psi}(\boldsymbol{\xi}_d)\right\}\\ &= \frac{k\exp[ik_z(\boldsymbol{\xi}_{d,\perp})z]}{k_z(\boldsymbol{\xi}_{d,\perp})}\iiint \tilde{O}_\perp(\boldsymbol{\xi}_{d,\perp} - \boldsymbol{\xi}_{i,\perp})\bar{O}_z(\pm k_z(\boldsymbol{\xi}_{d,\perp}) - \xi_{i,z})\hat{P}(\boldsymbol{\xi}_i)d^3\boldsymbol{\xi}_i.\end{aligned} \tag{19}$$

Since we assume the detector will be placed in the far-field, such that $|\tilde{\psi}|$ will be measured, we omit the $\exp[ik_z(\boldsymbol{\xi}_{d,\perp})z]$ phase factor for simplicity by choosing $z = 0$ as our reference plane.

As a second step, we may reduce the integral from 3D to 2D by performing the integral over $\xi_{i,z}$, remembering that $\hat{P} = \tilde{P}\delta_{ES}^+$ gives the Ewald Sphere delta function in a similar fashion to the previous step. We then gain another Jacobian factor and substitute $\xi_{i,z} = k_z(\boldsymbol{\xi}_{i,\perp})$. This gives us

$$\begin{aligned}\tilde{\psi}(\boldsymbol{\xi}_{d,\perp}; 0) &= \iint \frac{k^2}{\pm k_z(\boldsymbol{\xi}_{d,\perp})k_z(\boldsymbol{\xi}_{i,\perp})}\tilde{O}_\perp(\boldsymbol{\xi}_{d,\perp} - \boldsymbol{\xi}_{i,\perp})\bar{O}_z\left(\pm k_z(\boldsymbol{\xi}_{d,\perp}) - k_z(\boldsymbol{\xi}_{i,\perp})\right)\tilde{P}^+(\boldsymbol{\xi}_{i,\perp})d^2\boldsymbol{\xi}_{i,\perp}\\ &= \iint \tilde{O}_\perp(\boldsymbol{\xi}_{d,\perp} - \boldsymbol{\xi}_{i,\perp})\tilde{P}^+(\boldsymbol{\xi}_{i,\perp})d(\boldsymbol{\xi}_{d,\perp}, \boldsymbol{\xi}_{i,\perp})d^2\boldsymbol{\xi}_{i,\perp}.\end{aligned} \tag{20}$$

Here we may make the connection with the general scattering operator from Eq. (12): our expression now gives us an explicit solution for the S operator in terms of the object function O:

$$S(\boldsymbol{\xi}_\perp, \boldsymbol{\xi}'_\perp) = \frac{k^2}{\pm k_z(\boldsymbol{\xi}_\perp)k_z(\boldsymbol{\xi}'_\perp)}\tilde{O}_\perp(\boldsymbol{\xi}_\perp - \boldsymbol{\xi}'_\perp)\bar{O}_z\left(\pm k_z(\boldsymbol{\xi}_\perp) - k_z(\boldsymbol{\xi}'_\perp)\right). \tag{21}$$

Although the expression in Eq. (20) is, like our target of Eq. (18), an integral over two dimensions, it is not yet in the required form: the $\boldsymbol{\xi}_{d,\perp}$ and $\boldsymbol{\xi}_{i,\perp}$ coordinates still appear separately inside d. This prevents writing the expression as a pure convolution, where functions may only be evaluated at coordinate differences $\boldsymbol{\xi}_\perp - \boldsymbol{\xi}_{i,\perp}$ or at $\boldsymbol{\xi}_{i,\perp}$. Herein lies the core of the 2D approximation: to rewrite the near-convolutional form of Eq. (20) towards the purely convolutional form of Eq. (18) we must make further approximations on d, that allow us to either neglect its influence, or include it in the probe or object functions in the integral. We will now formulate some of these assumptions, which will later be used to derive conditions on the sample thickness.

The simplest assumption to make is to neglect the influence of d entirely;

$$d \approx 1, \tag{22}$$

which should hold for all $\boldsymbol{\xi}$ in the integral of Eq. (20). Although this way we ensure a reconstruction of the true lateral contrast, it also places the most stringent conditions on maximum thickness.

Optics EXPRESS

Since nearly equivalent assumptions exist which are much less strict, this assumption is not very practical and we will disregard it from further analysis.

A less strict assumption is produced by taking the coordinate functions at the central incoming and outgoing wavevectors, such that $\xi_i = \boldsymbol{k}_{i,0}$ corresponds to plane-wave illumination and $\xi_d = \boldsymbol{k}_{d,0}$ corresponds to a single pixel detector. Then we can substitute $k_z(\boldsymbol{\xi}_{d,\perp}) \approx k_{z,d,0}$ and $k_z(\boldsymbol{\xi}_{i,\perp}) \approx k_{z,i,0}$ into Eq. (20):

$$d(k_z(\boldsymbol{\xi}_{d,\perp}), k_z(\boldsymbol{\xi}_{i,\perp})) \approx d' = d(\boldsymbol{k}_{d,\perp,0}, \boldsymbol{k}_{i,\perp,0}), \tag{23}$$

where we denote d' to be our approximation for the true function d. Under this specific approximation, d' is simply a constant, so the transforms of the approximating functions O' and P' may be readily found to be

$$\tilde{O}' \propto \tilde{O}_\perp, \tilde{P}' \propto \tilde{P}^+, \tag{24}$$

where the effect of d' is taken as a simple proportionality constant. This proportionality constant may be exchanged between P' and O', however this ambiguity always exists for "blind" ptychography where both P and O are reconstructed [29]. The approximation we make here is valid so long as it does not lead to large changes in Eq. (20), i.e. as long as $d \approx d'$ over the entire domain of $\boldsymbol{\xi}_d$ and $\boldsymbol{\xi}_i$ in the integral. Because the demands this places on the variation of d are still significant, this will be referred to as the "strict" approximation. The strict approximation may be considered to be similar to approximating the depth effects for the various incoming and back-scattered plane-waves as if they all originated from the central plane-waves only, similar to the conventional approach in reflection ptychography, where the accumulated phase due to reflections at different depths is computed assuming a single incoming and reflected plane-wave.

By taking the central point in the angular distribution in just one of the two coordinates, we can make the previous assumption even less demanding. This means we take either $\boldsymbol{\xi}_{d,\perp} \approx \boldsymbol{k}_{d,\perp,0}$, which we will call the the relaxed detector case, or $\boldsymbol{\xi}_{i,\perp} \approx \boldsymbol{k}_{i,\perp,0}$, which we call the relaxed, illumination case. The dependence on the other coordinate is left unadjusted. Using these approximations, we can repeat our previous process to find functions O', P' which lead to equality between Eq. (18) and Eq. (20). All resulting approximations are summarized in Table 1.

Table 1. Three approximation cases for $d \approx d'$ which lead to equality between Eq. (18) and Eq. (20).

	Strict	Relaxed (detector)	Relaxed (illumination)
$\boldsymbol{\xi}_{i,\perp} \approx$	$\boldsymbol{k}_{i,\perp,0}$	not approximated	$\boldsymbol{k}_{i,\perp,0}$
$\boldsymbol{\xi}_{d,\perp} \approx$	$\boldsymbol{k}_{d,\perp,0}$	$\boldsymbol{k}_{d,\perp,0}$	not approximated
$d'(\boldsymbol{\xi}_\perp) =$	$d(\boldsymbol{k}_{d,\perp,0}, \boldsymbol{k}_{i,\perp,0})$	$d(\boldsymbol{k}_{d,\perp,0}, \boldsymbol{\xi}_\perp)$	$d(\boldsymbol{\xi}_\perp + \boldsymbol{k}_{i,\perp,0}, \boldsymbol{k}_{i,\perp,0})$
$\tilde{O}'(\boldsymbol{\xi}_\perp) \propto$	$\tilde{O}_\perp$	$\tilde{O}_\perp$	$\tilde{O}_\perp d'$
$\tilde{P}'(\boldsymbol{\xi}_\perp) \propto$	$\tilde{P}^+$	$\tilde{P}^+ d'$	$\tilde{P}^+$

It is important to note that the condition $d \approx d'$ controls the absolute variation of d over the sampled range, but does not by itself guarantee that the approximation it remains informative. In particular, if the central scattering vector $\pm\boldsymbol{k}_{d,0} - \boldsymbol{k}_{i,0}$ lies near a zero of $\bar{O}_z$, we have $d' = d(\boldsymbol{k}_{d,\perp,0}, \boldsymbol{k}_{i,\perp,0}) = 0$: the strict approximation becomes singular at the expansion point. The central contribution vanishes, while contributions away from $\boldsymbol{k}_{d,\perp,0}$ and $\boldsymbol{k}_{i,\perp,0}$ remain finite. Such a situation occurs if the specular reflection geometry corresponds to a destructive Bragg condition, where complex contributions to the scattering of the central wavevectors averages to precisely 0. In that regime, even a small absolute variation of $\bar{O}_z$, and by extension d, over the sampled domain can be large relative to the strict approximation itself, so higher-order terms in the variation of d are still relevant to the prediction of the total intensity.

Having formalized constraints on the variation of d in reciprocal space, we are now ready translate this to constraints on the spatial extent of the sample (i.e. the single layer thickness) in real space. We therefore choose a function that limits the object z-dependence in real space, for example a rectangle function of thickness t, such that $\bar{O}_z(\xi_z) = t\text{sinc}\,(t\xi_z)$. We find the maximum thickness t_{max} by demanding the argument of the sinc function to vary by much less than 2π within the domains of integration where d is assumed constant by the various approximations. We assume that $\bar{O}_z$ is the dominant factor leading to the variation of d', since $k_z(\boldsymbol{\xi}_\perp)$ only varies between 0 and 1 once over the domain of all possible $\boldsymbol{\xi}_\perp$, while $\bar{O}_z$ can have multiple minima an maxima in the same domain. Following this constraint we obtain for the maximum permissible thickness for the three cases:

The ranges of $\xi_{d,z}$ and $\xi_{i,z}$ for the transmission and reflection geometries are schematically shown in Fig. 3.

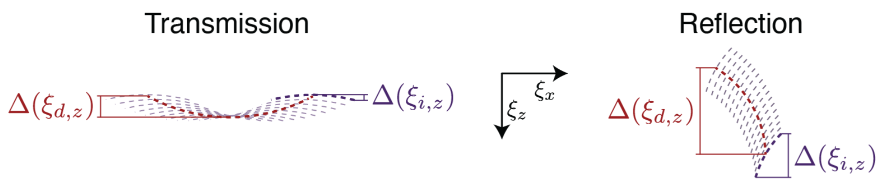

Fig. 3. The sampled ξ_z-ranges in the convolution of Eq. (14) for the transmission geometry (left) and reflection geometry (right).

We see that the two relaxed approximations differ only by swapping the distorting d between probe and object, depending on the domain where $d \approx d'$ is satisfied. For brevity, we will summarize these two cases in terms of a "limiting" coordinate, whichever places the least strict requirement on d:

$$\boldsymbol{\xi}_{\text{lim}} = \begin{cases} \boldsymbol{\xi}_d & \text{if } \Delta(\xi_{d,z}) < \Delta(\xi_{i,z}), \\ \boldsymbol{\xi}_i & \text{if } \Delta(\xi_{d,z}) \geq \Delta(\xi_{i,z}), \end{cases} \tag{25}$$

and so

$$t_{\text{lim}} \ll \frac{2\pi}{\Delta(\xi_{\text{lim},z})}. \tag{26}$$

Which coordinate is limiting determines where the distorting function f is expected to manifest itself. If $\boldsymbol{\xi}_{\text{lim}} = \boldsymbol{\xi}_d$, i.e. the illumination has the larger ξ_z-range and the detector has the smaller ξ_z-range, then the error should manifest itself in the probe function $P' = \tilde{P}^{+}d'$. Conversely, If $\boldsymbol{\xi}_{\text{lim}} = \boldsymbol{\xi}_i$, i.e. the detector has the larger ξ_z-range in Fourier space and the illumination has the smaller ξ_z-range, then the error will manifest itself in the object function $O' = \tilde{O}_\perp d'$. For standard ptychography experiments, one should expect $\boldsymbol{\xi}_{\text{lim}} = \boldsymbol{\xi}_i$, since the detector numerical aperture is typically larger than the illumination numerical aperture.

7. Reflection samples must be much thinner than transmission samples

We have seen that there are several thin-sample approximations that can be made, depending on the exact range of ξ_z values in the detector and illumination coordinates, which will be dictated by the experimental geometry. We can now apply the developed theory to predict the requirements of sample thickness on two different experimental geometries: reflection-mode and transmission-mode. We will show how the conditions from Table 2 lead to vastly different requirements on sample thickness, where the reflection geometry may require orders of magnitude smaller thicknesses.

In the transmission geometry, the z-component of the Fourier coordinates only arises due to the curvature of the Ewald sphere. Approximating the curvature as a parabolic (paraxial

Optics EXPRESS

Table 2. The maximally permissible thicknesses for the three approximation cases. $\Delta(\cdot)$ indicates the range of its argument, i.e. $\Delta(\boldsymbol{a}) = \max(\boldsymbol{a}) - \min(\boldsymbol{a})$.

	Strict	Relaxed (detector)	Relaxed (illumination)
$d \approx d'$ for	all $\xi_{d,\perp}$ and $\xi_{i,\perp}$	$\xi_{d,\perp}$ only	$\xi_{i,\perp}$ only
$t \ll$	$2\pi/\Delta(\pm\xi_{d,z} - \xi_{i,z})$	$2\pi/\Delta(\xi_{d,z})$	$2\pi/\Delta(\xi_{i,z})$

approximation), we therefore obtain

$$\frac{t_{\text{strict}}}{\lambda} \ll \frac{2}{\mathrm{NA}_i^2 + \mathrm{NA}_d^2}, \tag{27}$$

$$\frac{t_{\text{lim}}}{\lambda} \ll \frac{2}{\mathrm{NA}_{\text{lim}}^2}, \tag{28}$$

where we define $\mathrm{NA}_{\text{lim}} = \min(\mathrm{NA}_i, \mathrm{NA}_d)$ and t_{strict} and t_{lim} correspond to the maximal thicknesses from Table 2. It is worth noting that Eq. (28) has been previously derived in [6] for the case of small illumination NA.

For the specular reflection geometry the story is quite different: now the appearance of ξ_z in the diffraction integrals is dominated by the rotation of the Ewald sphere, and it is instead the curvature that may be neglected. This leads to

$$\frac{t_{\text{strict}}}{\lambda} \ll \frac{1}{2\sin(\theta_i)(\mathrm{NA}_i + \mathrm{NA}_d)} \tag{29}$$

$$\frac{t_{\text{lim}}}{\lambda} \ll \frac{1}{2\sin(\theta_i)\,\mathrm{NA}_{\text{lim}}}. \tag{30}$$

Note that the negligence of the Ewald sphere curvature is only valid when the rotation is the dominating contribution to $\Delta(\xi_z)$. The linear contribution starts to dominate when Eq. (28) is equal to Eq. (30), which for the relaxed case means $\theta_i \geq \frac{1}{4}\mathrm{NA}_{\text{lim}}$ with θ_i in radians. There is also a reflection geometry which illuminates directly perpendicular to the sample plane and detects directly reflected light, i.e. where $\theta_i = 0$, $\theta_d = \pi$. It is important to note that cases where $\theta_i = 0$, i.e. reflection ptychography under normal incidence, the limiting condition is again equivalent to the transmission case.

To assess the implications of the differences between a transmission and a reflection geometry, let us take a numerical example corresponding to a realistic scenario in Extreme Ultraviolet (EUV) reflection ptychography: $\mathrm{NA}_i = 0.05$, $\mathrm{NA}_d = 0.3$, $\theta_i = \theta_d = 60^\circ$. This example has been worked out in Table 3. The decrease of a factor 10 in the strict case and a factor 70 in the relaxed case in the example highlights the generally much more stringent thin sample conditions for reflection geometries as compared to transmission geometries. The large relative difference between the transmission and reflection geometries deserves particular emphasis: evidently, reflection geometries are much more sensitive to depth than their transmission counterparts. In addition to this specific case, t_{lim} is also shown in Fig. 4 for a variety θ_i and NA_{lim} values to serve as a reference for different geometries.

Table 3. The maximum thicknesses for an example geometry in EUV reflection ptychography, where $\theta_i = 60^\circ$, $\mathrm{NA}_i = 0.05$ and $\mathrm{NA}_d = 0.3$.

	Transmission	Reflection
t_{strict}	$\ll 22\lambda$	$\ll 1.7\lambda$
$t_{\text{lim}} = t_{\text{relaxed},i}$	$\ll 800\lambda$	$\ll 12\lambda$

Optics EXPRESS

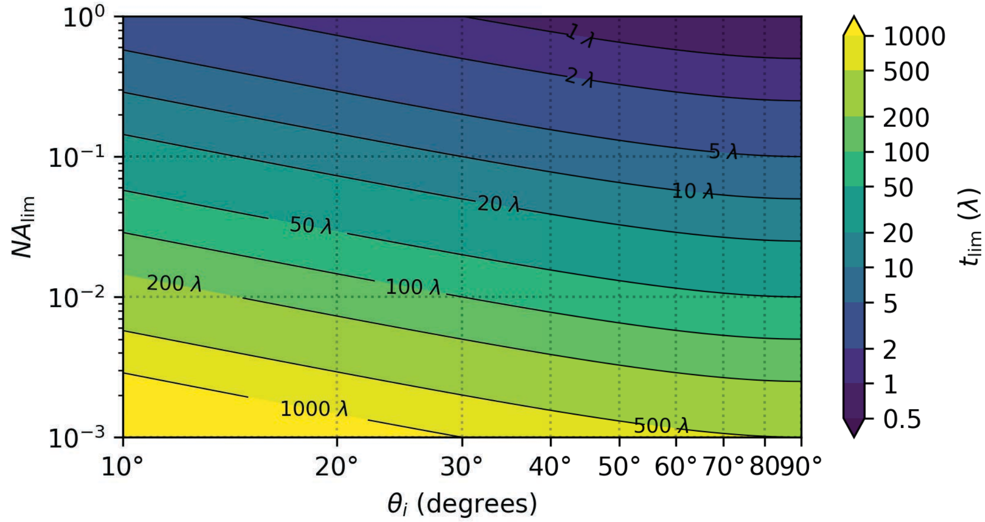

Fig. 4. The maximal allowable thickness t_{lim} for reflection geometries at an incident angle θ_i under the relaxed approximation. Note that most ptychography experiments will have $\text{NA}_{\text{lim}} = \text{NA}_i$.

8. Simulation verification

To verify the predictions from the theory, our approach will be to first simulate diffraction patterns from a ground-truth model which fits the assumptions made previously, such that the predictions on the sample thickness and expected errors should hold. Next, we reconstruct these simulated datasets using a simple two-dimensional ptychographic solver. By analyzing the resulting P' and O' in the two-dimensional case we can verify our model predictions. Additionally, we can study whether the model that includes the effects of depth is able to correct the distortions in the 2D reconstructions and can again reconstruct the ground truth values.

A simple numerical model that fits the theory from the previous chapter is generated by constricting the interaction scattering volume to two planes of constant z. This way, we are free to choose the lateral patterning $O_\perp$, but we fix the depth function $\bar{O}_z$ to

$$\begin{aligned} O_z(z) &= \delta(z) + \delta(z-t), \\ \bar{O}_z(\xi_z) &\propto \cos(\frac{1}{2}t\xi_z), \end{aligned} \tag{31}$$

With t again the thickness. We will refer to these reconstruction as the '2+1D'-case, since it includes both the lateral and axial dimensions, but the axial effects are handled differently from the lateral effects, i.e. they are not modeled by fully sampled arrays. The choice for the pair of delta functions is not coincidental: only for depth functions based on real-space delta functions it is possible to implement the ground truth of the theoretical model numerically in real-space without approximation. Other choices for $\bar{O}_z$ require exact computation of the integral in Eq. (20), which is numerically challenging since one cannot make use of the fast fourier transform to handle the convolution. We therefore proceed by taking the exit field to be the sum of the contributions from the $z = 0$ and $z = t$:

$$\psi(x, y) = \psi_t + \psi_b, \tag{32}$$

where

$$\psi_t = O_\perp(x, y)P(x, y), \tag{33}$$

$$\psi_b = \mathcal{P}^{-}_{-t}\{O_\perp(x,y)\mathcal{P}^{+}_{t}\{P(x,y)\}\}, \tag{34}$$

where $\mathcal{P}^{\pm}_{z}$ is the off-axis angular spectrum propagator [30] in the $\pm z$-direction for a distance z, remembering that the angular spectrum propagator is equivalent to the full 3D approach per Eq. (3) and Eq. (5). We note that this approach is simply an example implementation of the theoretical model that was derived in the previous chapters. As such, the assumptions the theoretical model was derived under, namely weak scattering and object separability, still hold for this implementation. The assumption of weak scattering allows for computation of the probe at the bottom layer without incorporating perturbations from the top layer. The separability assumption is not strictly required for the numerical model, it would for example be fine to choose a different lateral patterning $O_\perp$ for the bottom layer than for the top layer, however this would be contradictory to our goal of matching the numerical model to theoretical model.

All simulations were run in dimensionless units of length proportional to the wavelength. The probe was chosen as an elongated circular aperture, spanning roughly half the real space field-of-view of a single diffraction pattern, to ensure that $\mathrm{NA}_{\mathrm{lim}} = \mathrm{NA}_i$. Propagation to the detector was performed using a modified tilted forward model previously described in [20]. Reconstructions were performed on the simple two-dimensional datasets, with an initial probe conforming to the ground truth from the simulations, and an initial object set uniformly. Unless otherwise indicated, the probe was not included in the optimization, to keep the situation as close as possible to the theoretical description where we assume either O or P may receive the distortion due to $\bar{O}_z$. For more details on the simulation procedure we refer to the Supplement 1.

8.1. Reconstructed distortions in reflection ptychography

Firstly we assess the effect of the distortions by $\bar{O}_z$ on the reconstructed lateral patterning for two-dimensional reflection ptychography experiments. Simulations and reconstructions were performed for an incident angle $\theta_i = 60°$, such that $\cos(\theta_i) = 0.5$. t was varied in the range of $(0, 40\lambda)$ and $\mathrm{NA}_d = 0.3$ was chosen for the detector NA. For simplicity and due to its similarity with patterned nanostructures, the sample lateral patterning was chosen to be a binary, amplitude only function with $O_\perp = 1$ in the patterned part and 0 elswhere. The patterned part corresponded to a Siemens star pattern for easy resolution assessment. Reconstructions were performed using an automatic-differentiation based ptychography framework [31] built on the JAX library [32]. For more details on the optimization procedure, we refer to the Supplement 1.

The 2D reconstructions in reflection showed large, periodic variations in the residual loss after optimization with respect to the thickness, corresponding to a period of 1λ with the smallest residual loss at $t = n\lambda$ and the largest residual loss at $t = (n + 0.5)\lambda$ for integer n. These values correspond exactly to thicknesses which satisfy the destructive (high residual loss) and constructive (low residual loss) Bragg interference conditions for the zero-order specular reflection. In our three dimensional model, this may be understood as values where $\bar{O}_z$ is either 0 (destructive) or maximal (constructive) for $\boldsymbol{\xi}_\perp = (0, 0)$.

The Bragg condition also explains why elevated residual loss already appears at $t = 0.5\lambda$, even though the thin-sample bounds derived above are still satisfied. At this thickness, the strict approximation samples $\bar{O}_z$ at the central incoming and outgoing directions, where the specular term is at a Bragg minimum and the corresponding zeroth-order contribution vanishes. The measured intensity is nevertheless not zero, because the finite illumination and detection apertures still sample nearby off-axis scattering vectors for which $\bar{O}_z$ remains non-zero. The resulting dataset is therefore not incompatible with the thin-sample conditions; rather, it is a case where the zeroth-order strict approximation becomes poorly conditioned and the variation of $\bar{O}_z$ across the aperture becomes the dominant contribution.

The total intensity of the diffraction patterns shows a similar variation to the reconstructed error, such that one might be tempted to attribute the higher residual loss to a lower signal-to-noise ratio (SNR). We note however that these simulations were performed assuming theoretical ideal

Optics EXPRESS

conditions, without addition of noise or limitation of the dynamic range. This means that the signal to noise ratio is equal for all thicknesses, independent of the total intensity in the detected pattern, and therfore the distortions in the reconstructions are not caused by SNR variations.

The reconstructed O' values hardly show any effect of the distortion by $\bar{O}_z$ for most low thickness values, with the notable exception when the thickness is very close to a destructive Bragg condition. In that case, the average of the object function O' (corresponding to $\tilde{O}'(0,0)$) is nearly 0, with contrast only remaining near x-derivatives of the original object function O. This may be understood by linear approximation of the distortion function $\bar{O}$ in Fourier space with respect to ξ_x: $\bar{O}_z(\xi_\perp) \approx a\xi_x$, resulting in $O'(\boldsymbol{r}) \propto \frac{d}{dx}O_\perp(\boldsymbol{r})$. When further increasing the thickness to t, the reconstructed O' also exhibits clear errors for experiments in constructive Bragg conditions. These reconstructions are been shown in Fig. 5.

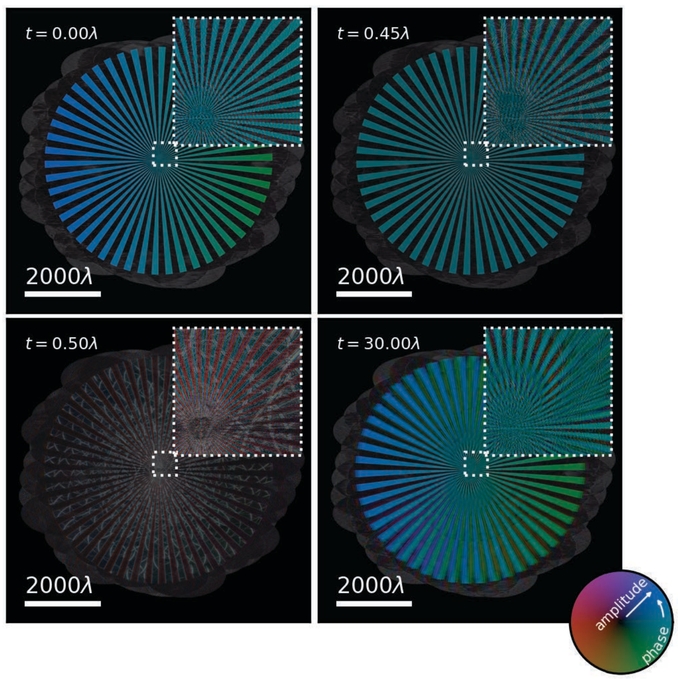

Fig. 5. The reconstructed two-dimensional function O' for 3D simulated data, given a true thickness value of (from left to right) 0, 0.45λ, a destructive Bragg condition at 0.5λ and a constructive Bragg condition at 30.0λ.

To verify the prediction of the distorting function $\bar{O}_z$, the Fourier transformed version of the reconstructed object $\tilde{O}'$ was compared to the reconstruction predicted by the approximations in Table 1. The predicted reconstruction is computed by a multiplication in the Fourier domain between the lateral funtion $\tilde{O}_\perp$ and the approximated error $\bar{O}_z$, so the real space O_z acts like a point-spread function on the true lateral object $O_\perp$. A comparison between the expected and the true reconstructions for a destructive Bragg thickness of 20.5λ shows excellent agreement between the prediction of the distortion and the reconstructed two-dimensional function, as can be seen in in Fig. 6.

8.2. Optimization of the 2+1D model

We have seen that two-dimensional reconstructions are not guaranteed to be sufficient for reconstructing weak-scattering samples, starting at thicknesses already corresponding to the first Bragg minimum. This raises the question if optimization of the 2+1D model will be able to

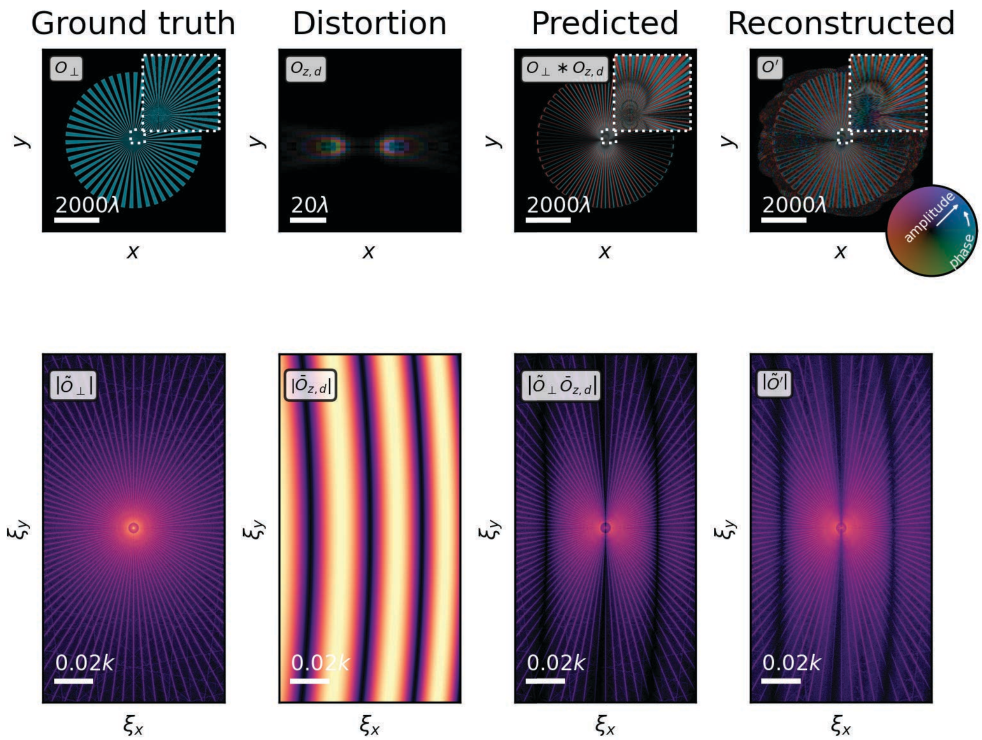

Fig. 6. A comparison between the real- and Fourier space representations of (from left to right), the ground truth lateral function $\tilde{O}_\perp(\boldsymbol{\xi})$, the approximation of the distorting function evaluated on the detection Ewald sphere $\bar{O}_{z,d}(\boldsymbol{\xi}) = \bar{O}_z(\pm k_z(\boldsymbol{\xi}_\perp + \boldsymbol{k}_{i,\perp,0}) - \boldsymbol{k}_{i,z,0})$, the ground truth after applying the predicted distortion ($\tilde{O}\,\bar{O}_{z,d}$), and the reconstructed object O'. The simulation was based on a thickness of 20.5λ, corresponding to a Bragg minimum condition, as may be seen by the line of $|\bar{O}_{z.d}|$ which passes through the center of the Fourier space.

correct the distortions that are clear in the two-dimensional case. Furthermore, it should be possible to optimize for the thickness if the initial guess is incorrect, since the 2+1D model is a function of the thickness t. To this end, another simulation was conducted to study optimization of the 2+1D model. This simulation was designed with the intention of accurately portraying realistic experimental conditions, instead of theoretically perfect ones. The probe was chosen based on a previous reconstruction of experimental data and Poisson noise was added to the detected diffraction patterns. The Poisson noise was based on a total illumination power of 5 μW at an EUV wavelength of 18.5 nm with a 100 ms exposure time, for an average photon count per pixel of $11.7 \cdot 10^4$ for a 1980x1980-pixel detector in the case of perfect reflection of the probe beam. The detected diffraction patterns were quantized to the range of a 14-bit detector. The initial guess for the object function was set to unity.

Firstly, we compare the case of the 2D to the 3D reconstructions in the Bragg destructive case, where the 2D reconstructions showed the most artifacts. As can be seen in Fig. 7(a), the errors in the lateral function that arise due to the destructive Bragg condition can be largely avoided when the 2+1D model is solved for, only parts in the edges of the field-of-view, where the object is illuminated by only a few scanning positions, still show some low-frequency deviations.

Another simulation was performed at the large ground-truth thickness of 30 λ, where the 2D models of the last sections also led to reconstruction errors near the higher spatial frequencies. Here, the initial guess for the reconstructed thickness t' was offset from the ground truth value of t.

Optics EXPRESS

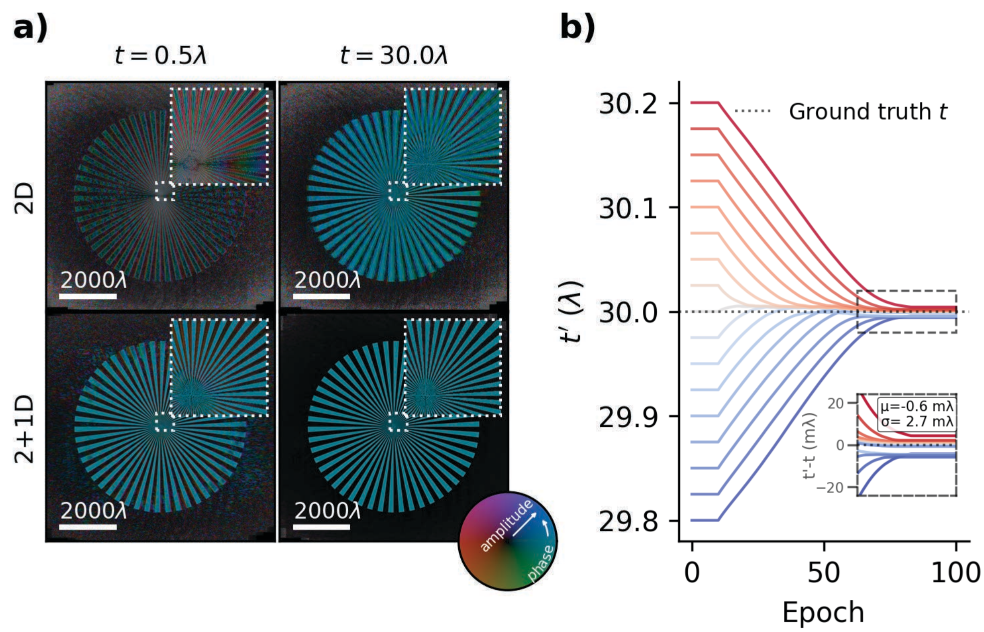

Fig. 7. a: The reconstructions of the two-dimensional model (top) versus the 2+1-dimensional model (bottom) for simulated data based on thicknesses of 0.5λ (left) and 30λ (right). b: The optimization progression of the reconstructed thickness parameter t' for the case of a true thickness t of 30λ, for varying initial guesses of t'. The inset is a y-scaled version of the full plot, indicating the mean from the ground truth μ and the standard deviation σ away from the ground truth value in the final 10 epochs.

Optimization of the thickness was enabled after 10 epochs to ensure stable reconstructions, while other reconstruction parameters were identical to the previous section. If the initial thickness was offset by more than roughly 0.2λ, optimization of the thickness would either stagnate or converge to a local minimum. The local minima seemingly appear for thicknesses at positions displaced by roughly a full wavelength from the true thickness. This may be explained by noting that for these thicknesses, the optimization most closely fits the Bragg minima and maxima to the nearest thickness where they more or less align with the data. For simulations with initial guesses inside of this domain of convergence, the thickness could reliably converge to the true value, as can be seen in Fig. 7(b). The final accuracy of the optimized thicknesses, measured as the root mean square deviation from the ground truth, was ± 2.7 mλ, or 50 pm for the simulation wavelength of 18.5 nm.

9. Discussion

The results as presented above clearly indicate that the developed theory may be used to assess the validity of the two-dimensional thin sample approximation in reflection ptychography, however it still relies on the assumptions of weak scattering and separability. For samples which satisfy these assumptions, we have derived practical limits on the sample thickness for which a 2D approximation is still valid. The theory additionally predicts the appearance of distortions in 2D reconstructions whenever the strictest thickness condition is not satisfied, thus extending the original theory of ptychography [6] to reflection geometries and making explicit the influence of thickness on its reconstructions. We confirmed the predicted distortions appear in simulation, thereby validating the predicted thickness limits. Finally, we demonstrate that inclusion of depth in the forward model corrects distortions that would be present if a 2D model is used. The incorporation of depth effects allows us to additionally optimize for the sample thickness for moderately incorrect initial guesses.

Plenty of research has been published which demonstrated experimentally that ptychography can be applied in a reflection geometry. Most published works meet the requirements on sample thickness dictated by relaxed thin sample approximation by reconstructing engineered samples with heights of only several wavelengths [4,5,7,8,11,12,14,15,17] or with very small limiting numerical apertures [21]. Our present efforts show that these demonstrations might not hold up when expanded to samples of greater thickness. Other works image samples where our developed theory should not be expected to apply, for example structures with small penetration depths compared to the wavelength [9,17], or substrates with very high reflectivity values [16]; all indications of the presence of strong scattering. In this work we also show that there are many thicknesses for which simple 2D models can provide reconstructions which are nearly indistinguishable from their ground-truth values; ptychography is evidently fairly robust with respect to noise sources and specific errors that do not fit into the original modeling. However, our present work shows that there is always a possibility that a previously unknown modeling inaccuracy gives rise to unexpected artifacts, especially when the reconstruction models build on theory for which it is not validated. As a more robust theory for reflection ptychography over extended depth ranges is currently not available, one should therefore always beware of the possibility that reconstructed features of interest are not physical, but instead arise from modeling inconsistencies.

A remaining question is whether the assumptions of weak scattering and separability made in this work are also valid in experimental settings where reflection ptychography is intended to be used; this work does not provide an answer to this question. One should note however that we have only extended the already existing theoretical framework that forms the basis of ptychography. In other words, if the theory as presented in this work is invalid for experimental use, because experiments of practical interest do not satisfy the assumptions of weak scattering and/or separability, then there is currently no available theory that is valid in describing the outcomes of such experiments. This work may be considered a first step towards the development of a theory of reflection ptychography that accurately models the inherent three-dimensional nature of the reflected field of samples which are more than several wavelengths thick.

10. Conclusion

This work demonstrates that application of the theory developed for transmission ptychography by performing two-dimensional reconstructions in reflection geometries at non-normal incident angles is not guaranteed to provide accurate reconstructions. If the measurement geometry and sample thickness are known, the distortion may be predicted using the developed theory. The distortion may be small for low thicknesses and away from Bragg minima, but whenever Bragg minima appear in the field-of-view of the detector, artifacts are bound to appear. It may take only a small change in modeling, namely inclusion of the correct depth effects in the propagation model, to prevent the distortions from appearing in the reconstruction outcome and thus to increase the range of sample thicknesses for which reflection ptychography may be safely applied. Whether or not the depth effects used in the simulations in this work are experimentally valid, their inclusion in the modeling gives the additional benefit of allowing one to reconstruct the feature thickness of binary lithographic samples from the propagation geometry alone. This hints at the potential use of reflection ptychography as a means for imaging depth-resolved samples directly from reflection-ptychographic data, without need for variation of the angle-of-incidence or spectral diversity. Although numerical reconstruction models must be extended from binary lithographic features to continuous depth profiles, this work still provides an exciting prospect that warrants further study.

Optics EXPRESS

Funding. Holland High Tech (22.0220).

Disclosures. WC: ASML Netherlands B.V. (E).

Data availability. Data underlying the results presented in this paper are available in Ref. [33], including notebooks to generate the figures and reproduce the simulations.

Supplemental document. See Supplement 1 for supporting content.

References

1. J. Bogdanowicz, A.-L. Charley, P. Leray, *et al.*, "3d Metrology and Inspection to Enable the Rise of Stacked Transistors, Wafers, and Chips," in *Metrology, Inspection, and Process Control XXXIX*, vol. 13426 (SPIE, 2025), pp. 8–15.
2. J. M. Rodenburg, A. C. Hurst, and A. G. Cullis, "Transmission Microscopy without Lenses for Objects of Unlimited Size," Ultramicroscopy **107**(2-3), 227–231 (2007).
3. A. M. Maiden and J. M. Rodenburg, "An Improved Ptychographical Phase Retrieval Algorithm for Diffractive Imaging," Ultramicroscopy **109**(10), 1256–1262 (2009).
4. D. F. Gardner, B. Zhang, M. D. Seaberg, *et al.*, "High Numerical Aperture Reflection Mode Coherent Diffraction Microscopy Using Off-Axis Apertured Illumination," Opt. Express **20**(17), 19050–19059 (2012).
5. M. D. Seaberg, B. Zhang, D. F. Gardner, *et al.*, "Tabletop Nanometer Extreme Ultraviolet Imaging in an Extended Reflection Mode Using Coherent Fresnel Ptychography," Optica **1**(1), 39–44 (2014).
6. J. M. Rodenburg and R. H. T. Bates, "The Theory of Super-Resolution Electron Microscopy Via Wigner-Distribution Deconvolution," Philos. Trans. Phys. Sci. Eng. **339**(1655), 521–553 (1992).
7. M. Zürch, C. Kern, and C. Spielmann, "Xuv Coherent Diffraction Imaging in Reflection Geometry with Low Numerical Aperture," Opt. Express **21**(18), 21131–21147 (2013).
8. B. Zhang, D. F. Gardner, M. H. Seaberg, *et al.*, "Ptychographic Hyperspectral Spectromicroscopy with an Extreme Ultraviolet High Harmonic Comb," Opt. Express **24**(16), 18745–18754 (2016).
9. E. R. Shanblatt, C. L. Porter, D. F. Gardner, *et al.*, "Quantitative Chemically Specific Coherent Diffractive Imaging of Reactions at Buried Interfaces with Few Nanometer Precision," Nano Lett. **16**(9), 5444–5450 (2016).
10. D. Mamezaki, T. Harada, Y. Nagata, *et al.*, "Imaging Performance Improvement of Coherent Extreme-Ultraviolet Scatterometry Microscope with High-Harmonic-Generation Extreme-Ultraviolet Source," Jpn. J. Appl. Phys. **56**(6S1), 06GB01 (2017).
11. C. L. Porter, M. Tanksalvala, M. Gerrity, *et al.*, "General-Purpose, Wide Field-of-View Reflection Imaging with a Tabletop 13 Nm Light Source," Optica **4**(12), 1552–1557 (2017).
12. R. M. Karl, G. F. Mancini, J. L. Knobloch, *et al.*, "Full-Field Imaging of Thermal and Acoustic Dynamics in an Individual Nanostructure Using Tabletop High Harmonic Beams," Sci. Adv. **4**(10), 4295 (2018).
13. Y. Nagata, T. Harada, T. Watanabe, *et al.*, "At Wavelength Coherent Scatterometry Microscope Using High-Order Harmonics for EUV Mask Inspection," Int. J. Extrem. Manuf. **1**(3), 032001 (2019).
14. M. Tanksalvala, C. L. Porter, Y. Esashi, *et al.*, "Nondestructive, High-Resolution, Chemically Specific 3d Nanostructure Characterization Using Phase-Sensitive EUV Imaging Reflectometry," Sci. Adv. **7**(5), eabd9667 (2021).
15. Y. Esashi, N. W. Jenkins, Y. Shao, *et al.*, "Tabletop Extreme Ultraviolet Reflectometer for Quantitative Nanoscale Reflectometry, Scatterometry, and Imaging," Rev. Sci. Instrum. **94**(12), 123705 (2023).
16. H. Lu, M. Odstrčil, C. Pooley, *et al.*, "Characterisation of Engineered Defects in Extreme Ultraviolet Mirror Substrates Using Lab-Scale Extreme Ultraviolet Reflection Ptychography," Ultramicroscopy **249**, 113720 (2023).
17. Y. Shao, S. Weerdenburg, J. Seifert, *et al.*, "Wavelength-Multiplexed Multi-Mode EUV Reflection Ptychography Based on Automatic Differentiation," Light: Sci. Appl. **13**(1), 196 (2024).
18. M. Tanksalvala, A. Kos, J. Wisser, *et al.*, "Element-Specific High-Bandwidth Ferromagnetic Resonance Spectroscopy with a Coherent Extreme-Ultraviolet Source," Phys. Rev. Appl. **21**(6), 064047 (2024).
19. P. S. Jørgensen, L. Besley, A. M. Slyamov, *et al.*, "Hard X-Ray Grazing-Incidence Ptychography: Large Field-of-View Nanostructure Imaging with Ultra-High Surface Sensitivity," Optica **11**(2), 197–204 (2024).
20. S. Senhorst, Y. Shao, S. Weerdenburg, *et al.*, "Mitigating Tilt-Induced Artifacts in Reflection Ptychography via Optimization of the Tilt Angles," Opt. Express **32**(25), 44017–44030 (2024).
21. P. Myint, A. Tripathi, M. J. Wojcik, *et al.*, "Three-Dimensional Hard X-ray Ptychographic Reflectometry Imaging on Extended Mesoscopic Surface Structures," APL Photonics **9**(6), 066118 (2024).
22. D. Guenzing, D. Y. Sasaki, A. S. Ditter, *et al.*, "Soft X-ray Reflection Ptychography," arXiv (2026).
23. Y. Gao, Q. You, P. Lu, *et al.*, "Interface and Spectrum Multiplexing Ptychographic Reflection Microscopy," Opt. Lasers Eng. **193**, 109076 (2025).
24. J. W. Goodman, *The Angular Spectrum and Its Physical Interpretation* (McGraw-Hill, 1996), pp. 55–65.
25. L. Onural, "Impulse Functions over Curves and Surfaces and Their Applications to Diffraction," J. Math. Anal. Appl. **322**(1), 18–27 (2006).
26. R. Bracewell, *The Projection-Slice Theorem* (Springer US, Boston, MA, 2003), pp. 493–504.
27. E. Wolf, "Three-Dimensional Structure Determination of Semi-Transparent Objects from Holographic Data," Opt. Commun. **1**(4), 153–156 (1969).
28. K. C. Zhou, R. Qian, A.-H. Dhalla, *et al.*, "Unified K-Space Theory of Optical Coherence Tomography," Adv. Opt. Photonics **13**(2), 462–514 (2021).

Optics EXPRESS

29. A. Fannjiang and P. Chen, "Blind Ptychography: Uniqueness and Ambiguities," Inverse Probl. **36**(4), 045005 (2020).
30. Y.-H. Kim, C.-W. Byun, H. Oh, *et al.*, "Off-Axis Angular Spectrum Method with Variable Sampling Interval," Opt. Commun. **348**, 31–37 (2015).
31. S. Senhorst, "Ptyrax: A Differentiable Optics Simulation and Reconstruction Toolbox," Guthub, 2026 https://github.com/ssenhorst/ptyrax.
32. J. Bradbury, R. Frostig, P. Hawkins, *et al.*, "Jax: Composable Transformations of Python+NumPy Programs," Guthub, 2018 http://github.com/jax-ml/jax.
33. S. Senhorst, "Data supporting the publication: The 2D approximation quickly breaks down in reflection ptychography," Delft University of Technology 2026 https://dx.doi.org/10.4121/1fd1f6e7-349d-4805-a522-ee6e02afdb1a.